A Two Pressure Numerical Model of Two Fluid Mixing*

J. Glimm[§¶], H. Jin[§†], M. Laforest[§‡],
F. Tangerman[§], Y. Zhang[§]
[§]Department of Applied Mathematics and Statistics
University at Stony Brook
Stony Brook, NY 11794-3600
[¶]Center for Data Intensive Computing
Brookhaven National Laboratory
Upton, NY 11793-6000

January 23, 2003

Abstract

We present a numerical model of two fluid mixing based on hyperbolic equations having complete state variables (velocity, pressure, temperature) for each fluid. The model is designed for the study of acceleration driven mixing layers in a chunk mix regime dominated by large scale coherent mixing structures. The numerical solution of the model is validated by comparison to the incompressible limit. For the purpose of this comparison, we present a newly obtained analytic solution of the pressure equation for this model and an analytic constraint derived from the asymptotic limit of the compressible pressures, which determines uniquely the incompressible pressure solution. The numerical solution is also validated by a mesh convergence study.

*Supported in part by the U.S. Department of Energy DE-FG02-90ER25084, DE-FG02-98ER25363, DE-FG03-98DP00206, the National Science Foundation DMS-0102480, the Army Research Office grant DAAG19-01-0642 and Los Alamos National Laboratory.

†Supported in part by the Clay Mathematics Institute.

‡Supported in part by Le Fonds pour la Formation de Chercheurs et l'Aide à la Recherche (FCAR), Canada.

Keywords: multiphase flow, Rayleigh-Taylor instability.

1 Introduction

1.1 Fluid Mixing

Fluid mixing is important to technology, for example in pipeline flow and the performance of inertial confinement fusion reactors; it is important to the description of natural phenomena, as in meteorological temperature inversion driven updrafts and the geological evolution of salt dome formations; it is important to basic science in the evolution of supernova explosions. Fluid mixing is a multiscale phenomena, with active length scales from the submillimeter microscale of diffusive mixing to laboratory, geophysical or astrophysical scales of macroscopic flow. It is neither possible nor desirable to simulate all fine details accurately. There are neither the computer resources nor the initialization data to allow resolution of fine details, while for many purposes statistical averages at a macroscopic level are sufficient, and offer a more understandable description of the multifluid behavior. For this reason we seek averaged, or coarse grained equations, to describe the flow behavior of a multifluid mixture without direct simulation of all its microscopic details.

From the point of view of averaged equations, a multifluid mixture is a complex fluid with extra internal degrees of freedom. Starting from hyperbolic microscopic equations of two immiscible fluids, we consider averaged equations which are also hyperbolic, and which thus have only real characteristic speeds. The derivation of averaged equations leads to undefined averages of products or nonlinear functions of the primitive variables. These quantities must be modeled, *i.e.* expressed approximately as a function of the averaged flow quantities directly, to close the system of equations. Closure is a physics level identity, independent of the averaged governing equations. It restricts the applicability of the resulting system to the specific flow regime for which this identity has an approximate experimental validity. Multifluid flows possess a number of distinct flow regimes, which call for distinct closures, further complicating their study.

We are concerned with chunk mix [6, 9], a term we have introduced to describe a flow regime characterized by large scale coherent mixing structures (bubbles of light fluid, *etc.*), on the order of the thickness of the mixing

zone, and by short time scales, so that relaxation terms are omitted [3, 26, 27, 29, 6]. Alternate models and closures are presented in [41, 17, 44]. Averaged flow models differ primarily in the order of statistical moments carried as dependent solution variables (we use a first moment closure), in the completeness of the multiphase treatment (we use a fully multiphase formulation in that no fluid variables are shared, or averaged in common between the phases), and in the choice of specific closures, which usually correspond to some specification of the flow regime.

The closure used here is based on an assumed absence of internal length scales within the mixing zone, which is a mixing zone homogeneity assumption. It assumes independent thermodynamic variables (pressures and temperatures) for each phase, in addition to independent velocities. Its applicability includes rapid acceleration driven mixing processes for a chunk flow regime. For this purpose, we omit relaxation source terms which equilibrate pressures and velocities between the phases. We refer to [6] and the references therein for more information on this model and its closure assumptions.

The main result of this paper is the presentation in §2 of a numerical algorithm for the solution of the chunk mix multiphase fluid flow model with explicit tracking of the interface between the pure and multifluid regions. In §3 we find a closed form solution for the incompressible 1D pressure of this model, thereby completing the closed form solution of the incompressible 1D equations [28].

The model depends on the motions $Z_k(t)$ of the edges of the mixing zone. Since the Z_k are not well characterized for compressible flows, we explore the dependence of the solution on the Z_k. In fact, most of the solution variables, suitably scaled, are nearly independent of the Z_k. This is not the case for the pressure differences. These differences appear in the exact (momentum) equation for the edge motion. In §4.1, this fact is further related to the modeling of the drag and added mass terms in phenomenological buoyancy drag equations for the edge motion. The connection of the pressure difference to key terms in these buoyancy drag equations provides a physical basis for the sensitive dependence of the pressure difference on the edge motion.

Comparison to the analytic solution allows a numerical study of the incompressible limit for compressible flows, as a validation test of the numerical algorithm presented here. See §4.2. Validation of the algorithm is also performed in §4.3 through mesh convergence studies. Averaging of nonlinear equations, even the averaging of equations in conservation form, often leads to nonconservative equations. The present equations are an example. For

such equations, the mesh refinement required for accurate solution of the equations is an important consideration. We show mesh convergence beginning at a mesh level having between 8 cells (at the problem initialization) to 25 cells (at the time used for mesh convergence) within the mixing zone.

1.2 A Two Pressure Two Fluid Flow Model

We are concerned with the dynamic growth of a thin mixing layer formed at the interface between two fluids, and embedded in a larger flow field. Random perturbations on the interface grow due to fluid instabilities and evolve into a complex flow microstructure, to give rise to the mixing zone. We are here concerned with acceleration driven mixing. The averaging process used to define the model equations can be thought of as a local spatial or temporal average, or as an ensemble average, with respect to an ensemble of random initial conditions.

Within each realization the evolution of the interface is chaotic; at time t, the same space point may be occupied by fluid 1 or fluid 2, depending upon the position of the interface in that realization. Several realizations lead to the consideration of a mixed zone of fluids where, on average, one finds fluid k at a given point p only a fraction $\beta_k = \beta_k(t, p)$ of the ensemble total. Clearly, $\beta_k = 1$ corresponds to a pure fluid region, where there is no mixture at all, a situation that happens away from the interface of all realizations of the ensemble. Evidently,

$$\beta_1 + \beta_2 = 1 \, .$$

We parameterize the fluids by the discrete index k, $k = 1, 2$, and let β_k, ρ_k, $\vec{v}_k$, p_k and e_k be the volume fraction, density, velocity, pressure and total energy of fluid k, respectively. The model we study is defined by the system

of equations

$$
\begin{aligned}
\partial_t \beta_k &= -\vec{v}^* \cdot \nabla \beta_k \ , \\
\partial_t \rho_k + \nabla \cdot (\rho_k \vec{v}_k) &= -\rho_k \frac{(\vec{v}_k - \vec{v}^*)}{\beta_k} \cdot \nabla \beta_k \ , \\
\partial_t (\rho_k \vec{v}_k) + \nabla \cdot (\rho_k \vec{v}_k \otimes \vec{v}_k) + \nabla p_k &= -\rho_k \vec{v}_k \frac{(\vec{v}_k - \vec{v}^*)}{\beta_k} \cdot \nabla \beta_k \\
&\quad - \frac{(p_k - p^*)}{\beta_k} \nabla \beta_k + \rho_k \vec{g} \ , \qquad (1) \\
\partial_t (\rho_k e_k) + \nabla \cdot (\rho_k e_k \vec{v}_k) + \nabla \cdot (p_k \vec{v}_k) &= -\rho_k e_k \frac{(\vec{v}_k - \vec{v}^*)}{\beta_k} \cdot \nabla \beta_k \\
&\quad + \frac{((p\vec{v})^* + p^* \vec{v}_k - 2 p_k \vec{v}_k)}{\beta_k} \cdot \nabla \beta_k \\
&\quad + \rho_k \vec{v}_k \cdot \vec{g} \ ,
\end{aligned}
$$

proposed in [3, 26, 27, 29, 6]. Here, $\vec{g}$ is the gravity and $\vec{v}^*$, p^* and $(p\vec{v})^*$ represent averages to be modeled by a closure expression,

$$
\vec{v}^* = \mu_1^v \vec{v}_2 + \mu_2^v \vec{v}_1 \ , \qquad (2)
$$

$$
p^* = \mu_1^p p_2 + \mu_2^p p_1 \ , \qquad (3)
$$

$$
(p\vec{v})^* = \mu_1^p p_2 \vec{v}_2 + (1 - \mu_1^p - \mu_2^v) p_1 \vec{v}_2 + \mu_2^v p_1 \vec{v}_1 \ . \qquad (4)
$$

The coefficients μ_k^v and μ_k^p can be proved quite generally to define convex sums, so that $\mu_1^q + \mu_2^q = 1$, $\mu_k^q \geq 0$, $q = v, p$ [28]. These coefficients are assumed to depend on the volume fraction β_k and t only. Boundary conditions at the edge of the mixing zone imply

$$
\mu_k^q(t, \beta_k) = \frac{\beta_k}{\beta_k + d_k^q(t) \beta_{k'}} \ , \quad q = v, \ p \, , \qquad (5)
$$

where $k' = 3 - k$ is the complimentary index to k and the d's satisfy $d_1^q d_2^q = 1$.

Restricting the model to one spatial dimension z measuring height, let $z = Z_k(t)$ be the edge of the mixing zone where β_k vanishes. As a convention, the pure fluid region for fluid 1 will be located above the pure fluid region for fluid 2. Henceforth, we will assume that the mixing zone is expanding at both edges, *i.e.*, $(-1)^k \dot{Z}_k(t) \geq 0$, and set $V_k = |\dot{Z}_k(t)|$. In one spatial dimension, the constitutive factor d_k^v was shown [33] to be a z-dependent ratio of volume creation terms for the two multiphase species, independent of any closure

assumptions. As a condition of closure, we assume d_k^v is independent of z, and obtain

$$d_k^v(t) = \frac{\displaystyle\int_{Z_k}^{Z_{k'}} \frac{\partial v_{k'}}{\partial z} + \frac{1}{\rho_{k'}} \frac{D_{k'}\rho_{k'}}{Dt}\, dz}{\displaystyle\int_{Z_k}^{Z_{k'}} \frac{\partial v_k}{\partial z} + \frac{1}{\rho_k} \frac{D_k\rho_k}{Dt}\, dz} \ . \tag{6}$$

Refer to [24]. Here $D_k/Dt \equiv \partial/\partial t + v_k \partial/\partial z$ denotes the phase k convective derivative. The formula (6) defines the constitutive law as a function of the solution variables. In the weakly compressible limit, a perturbative analysis [33, 24] is applied to (6). This analysis supplies new information on incompressible pressures, which appear in second order in the Mach number in this expansion. From this analysis, we see [33] that underdetermination of the incompressible pressure is resolved by information supplied from the weakly compressible theory. The choice for the pressure closure

$$d_k^p = \rho_{k'}/\rho_k \tag{7}$$

appears quite naturally.

The system (1) is missing one condition at each edge $z = Z_k(t)$ of the mixing zone. Each missing condition is associated with a missing characteristic at the Z_k boundary. For the fluid with vanishing β_k, the sonic characteristic entering from the $\beta_k = 0$ side is missing. This missing information is supplied by the edge acceleration, $\ddot{Z}_k(t)$.

Thus we regard the edge positions $Z_k(t)$ as input, or data, which complete the specification of the model, or close it. We appeal to the buoyancy drag model (see [29] and references therein) to provide the $Z_k(t)$. In this sense we separate and almost totally decouple the complete multiphase model into distinct edge and interior models, with the edge model completing the closure of the entire model. Many authors do not decouple this analysis, and consider logically linked edge and interior equations. To the authors, the separation of these two distinct issues into two distinct models appears to be advantageous or at least harmless. With the mixing zone edge accelerations given and constitutive laws (6) and (7), the model has no adjustable parameters.

The mixing zone edge information will be supplied through a phenomenological buoyancy drag ODE to specify the edge accelerations,

$$(-1)^k \frac{d^2 Z_k(t)}{dt^2} = Ag - \frac{\rho_{k'}}{\rho_k + \rho_{k'}} C_k \frac{V_k^2}{|Z_k|} \ , \tag{8}$$

where the Atwood number $A = \frac{\rho_2 - \rho_1}{\rho_2 + \rho_1}$. Equations of the general form (8) are known as buoyancy-drag equations, and have been considered by a number of authors [31, 1, 7, 14, 38]. A systematic error [1, 14] has been the use of the displacing fluid density ρ_k in the numerator of the last term of (8). See [36] for correct discussion of drag. This error was corrected in [7] and subsequently in [38]. In the absence of this correction, a singular drag coefficient is required for $A = 1$. Given (8) and the self similar solution $Z_k = (-1)^k \alpha_k A g t^2$ for steady acceleration (Rayleigh-Taylor) mixing, there is a unique, one to one correspondence between C_k and α_k. For example

$$C_1 = \frac{1/\alpha_1 - 2}{2(1+A)} \,, \tag{9}$$

$$\alpha_1 = \frac{1}{2[1 + C_1(1+A)]} \tag{10}$$

so that with $\alpha_1 = 0.06$, C_1 varies by a factor of 2 from $C_1(A = 0) = 9$ to $C_1(A = 1) = 4.5$. We fit the available data on α_1, which does not show a significant trend in its dependence on A, and regard (9) as a definition of C_1. See Appendix A for the α_1 data.

The buoyancy drag equations (8) used to specify the edge equations depend parametrically on the Atwood number, and thus on the local density field. For (nearly) incompressible flow, the Atwood number can be specified from $t = 0$ data, and in this case the edge equations (buoyancy drag) and interior equations (1) decouple. In the general (compressible) case, the boundary Atwood number depends on the solution of the interior equations, so that the coupling between the edge equations and the interior is weak but nonzero.

The vertical length $|Z_k|$ in (8) is replaced in [38] with a horizontal length, the wave length λ. For this reason, the evaluation of α_1 in terms of C_1 in [38] depends on an additional ratio: the bubble height to bubble width ratio to convert a horizontal to a vertical length; whereas this ratio is not needed in [7]. The treatment of [38] assumes that the drag coefficient $C_1 \equiv 2\pi$ is independent of the Atwood number leading to a calculated value of α_1 varying from $\alpha_1 = 0.065$ at $A = 0$ to $\alpha_1 = 0.05$ at $A = 1$. After adjustment in [8] for the factor $\lambda/|Z_1| = 3$, so that λ appears in the denominator of the decay term (8), C_1 in [7] varies by a factor of 2, from 3 for $A = 0$ to 1.5 for $A = 1$, assuming $\alpha_1 = 0.05$. The experimental data shows no clear trend in the A dependence of α_1, so that a constant α_1 appears to be a

better interpretation of the experimental facts than is a constant C_1. The theoretically determined [8] value for $\lambda/|Z_1| = 3$ lies in the middle of the experimental values, whereas the value $\lambda/|Z_1| = 1.5$ of [38] is outside the experimental range. For this reason the drag coefficients from [7] and [38] do not agree.

We now describe the specific configuration to feature in our analysis and simulation. Suppose a slab of heavy fluid of density ρ_2 lies beneath a slab of light fluid of density $\rho_1 < \rho_2$, separated by an interface. This configuration is then accelerated downwards with an acceleration larger than the earth gravity, effectively reversing the direction of gravity. In the following, the fluids occupy a container $[0,1] \times [-1,1]$ with periodic boundary conditions in the horizontal direction. We impose zero velocity conditions at the upper boundary $z = 1.0$ and constant pressure conditions at the lower boundary $z = -1.0$ for our incompressible calculations. For the compressible calculations, we impose a rigid wall at the top, $z = 1.0$, and outflow boundary conditions connecting to a fixed ambient state at $z = -1.0$.

2 The Numerical Algorithm

The algorithm presented in this section is the extension of the front tracking algorithm [20, 21, 23, 22, 25, 30] to the two fluid mixture model (1). It is developed for two spatial dimensions, but is tested here for one dimensional flows only. Thus, the mixing zone edges $Z_k(t)$ needed to close the model can be used without transverse spatial dependence.

Front tracking is a numerical method in which selected waves are explicitly represented in the discrete form of the solution. Examples include shock waves, contact discontinuities, and material interfaces. Other waves, such as leading and trailing edges of rarefaction waves, have continuous states but jumps in their first derivatives. Tracked waves are propagated using the appropriate equations of motion for the given model. For example, if the system of equations consists of a set of hyperbolic conservation laws, $\mathbf{u}_t + \nabla \cdot \mathbf{f} = \mathbf{h}$, then the instantaneous velocity s of a discontinuity surface satisfies the Rankine-Hugoniot equations, $s\,[\mathbf{u}] = [\mathbf{f}] \cdot \mathbf{n}$. Here $\mathbf{n}$ is the unit normal to the discontinuity surface. During a time step propagation, the type of a wave, and the flow field in a neighborhood of the wave determine a local time integrated velocity for each point on the wave in the direction normal to the wave front. Wave propagation consists of moving each point a

distance $s\Delta t$ in the normal direction as well as computing the time updated states at the new position. Tracking preserves the mathematical structure of the discontinuous waves by maintaining the discrete jump at the wave front, thus eliminating numerical diffusion. It also allows for the direct inclusion of the appropriate flow equations for the wave front in the numerical solution. The stencils used for the update of the interior states which are irregular due to overlap with the front, are extended with ghost cells [25] to consist of state values from only one side of the front.

A tracked wave, known as a front (or, in 2D, a curve), is a piecewise linear representation of a physical wave, which is embedded in the underlying finite difference rectangular grid. A curve (or front) is a set of piecewise linear segments, called bonds. Each bond connects two points located at its two ends. Stored with each point are two states to represent the discontinuity across the wave. An orientation is given along the curve so that we may speak of the left and right states at a point. Propagation of the front can be defined as updating the position of each point on the front and updating the corresponding left and right states associated to it at a new time $t + \Delta t$. Operator splitting, in the rotated tangential normal coordinate system $(\vec{T}, \vec{N})$, allows separate propagation steps in directions normal to and tangent to the front. The tangential propagation is performed on each side of the front followed by the normal propagation. Since the solution is smooth during the tangential propagation, a convenient finite difference scheme, such as Lax-Wendroff, can be used to update the states at each point on the front. Notice that tangential propagation of points on the front is equivalent to remeshing of the front, in the limit $\Delta t \to 0$, so it is not essential to move these points during the tangential update.

On the computational domain we find a fixed rectangular computational grid, and an independently gridded lower dimensional front. This front is comprised of the mixing zone edges. Its mesh size is of the order of magnitude of the spacing in the rectangular grid. The complement of the front consists of either single phase or two phase fluids. Fluid states are assumed to vary smoothly within the closure of each component.

The data for the numerical solution consist of a (single or two phase) fluid state attached to every gridblock center, representing the average fluid state in the block and a (single or two phase) fluid state at each of the two sides of the front at any front grid point. These data, together with the choice of an interpolation method, determine the (single or two phase) fluid state at any point in any component, and thus the numerical solution.

2.1 Propagation of Front Points

Point propagate is a basic front tracking operation; for the gas dynamical version, see [10]. This operator computes the time-advanced position and state of the front. The currently implemented algorithm uses local dimensional splitting to decompose the equations of motion into components normal and tangential to the interface. Let $\vec{N}$, $\vec{T}$ be the normal and tangential unit vectors at some point on the front. Then $\vec{v_k}$ can be rewritten as $\vec{v}_k = v_k^N \vec{N} + v_k^T \vec{T}$, $\vec{v^*} = v_N^* \vec{N} + v_T^* \vec{T}$ and $\vec{g} = g_N \vec{N} + g_T \vec{T}$. The projection of the equations (1) onto the normal direction can be written as

$$
\begin{aligned}
\partial_t \beta_k &= -v_N^* \frac{\partial \beta_k}{\partial N} \ , \\
\partial_t \rho_k + \frac{\partial \rho_k v_k^N}{\partial N} &= -\rho_k \frac{(v_k^N - v_N^*)}{\beta_k} \frac{\partial \beta_k}{\partial N} \ , \\
\partial_t (\rho_k v_k^N) + \frac{\partial}{\partial N}(\rho_k v_k^N v_k^N) + \frac{\partial p_k}{\partial N} &= -\rho_k v_k^N \frac{(v_k^N - v_N^*)}{\beta_k} \frac{\partial \beta_k}{\partial N} \\
&\quad - \frac{(p_k - p^*)}{\beta_k} \frac{\partial \beta_k}{\partial N} + \rho_k g_N \ , \\
\partial_t (\rho_k v_k^T) + \frac{\partial}{\partial N}(\rho_k v_k^T v_k^N) &= -\rho_k v_k^T \frac{(v_k^N - v_N^*)}{\beta_k} \frac{\partial \beta_k}{\partial N} \ , \\
\partial_t (\rho_k e_k) + \frac{\partial}{\partial N}(\rho_k e_k v_k^N) + \frac{\partial}{\partial N}(p_k v_k^N) &= -\rho_k e_k \frac{(v_k^N - v_N^*)}{\beta_k} \frac{\partial \beta_k}{\partial N} \\
&\quad + \frac{((p v_N)^* + p^* v_k^N - 2 p_k v_k^N)}{\beta_k} \frac{\partial \beta_k}{\partial N} \\
&\quad + \rho_k v_k^N g_N \ .
\end{aligned}
\tag{11}
$$

Figure 1a shows the basic stencil of states used to compute the contribution to the normal component of flow. The states sl_0 and sr_0 denote the left and right states at the point to be propagated. States sl_i and sr_i are interpolated at distances Δn in the direction normal to the front. The projection of these states onto the line normal to the front is used to compute the interface velocity at the point and a pair of time updated left and right states at the front.

The system (11) is hyperbolic, with eigenvalues $\lambda^* = v_N^*$, $\lambda_k^{\pm} = v_k^N \pm c_k$, and $\lambda_k^0 = v_k^N$, corresponding respectively to characteristics C^*, $C_k^{\pm}$, and C_k^0. The λ_k^0 eigenvalue has multiplicity two, arising in both the tangential velocity

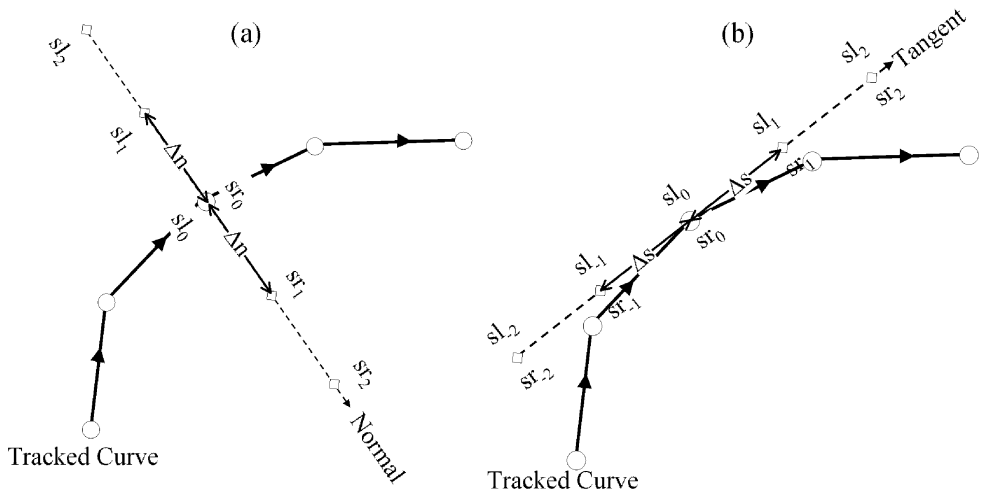

Figure 1: A schematic showing the stencil of states used in propagating a front point. For simplicity the diagram is shown for two space dimensions. The normal propagate stencil is shown in (a), while (b) shows the stencil used in the tangential update.

and energy equations in (11). Here c_k is a macroscopic sound speed. The characteristic equations of the system (11) are

$$(d\beta_k)_{C^*} = 0 \ , \tag{12}$$

$$(\xi_k^0 d\beta_k - c_k^2 d\rho_k + dp_k)_{C_k^0} = 0 \ , \tag{13}$$

$$(dv_k^T)_{C_k^0} = 0 \ , \tag{14}$$

$$(\xi_k^\pm d\beta_k \pm \rho_k c_k (dv_k^N - g_N dt) + dp_k)_{C_k^\pm} = 0 \ , \tag{15}$$

with

$$\xi_k^0 = \frac{W_k - \rho_k c_k^2 (v_k^N - v_N^*)}{\beta_k (v_k^N - v_N^*)} \ , \tag{16}$$

$$\xi_k^\pm = \frac{W_k \pm c_k (p_k - p^*)}{\beta_k (v_k^N \pm c_k - v_N^*)} \ , \tag{17}$$

$$W_k = (\gamma_k - 1) \left[\rho_k \epsilon_k (v_k^N - v_N^*) + p_k v_k^N - (p v_N)^* \right] \ . \tag{18}$$

Let Z_1^n be the bubble (vanishing light fluid) mixing zone edge position, Z_2^n be the spike (vanishing heavy fluid) mixing zone edge position, $(v_1^N)_{01}^n$, $(v_2^N)_{02}^n$ be the normal velocities of fluid 1 and fluid 2 at the corresponding positions Z_1^n and Z_2^n at time t^n. The edge position Z_k^{n+1} at the next time level t^{n+1} is updated using

$$Z_k^{n+1} = Z_k^n + (v_k^N)_{0k}^n \vec{N}_k \Delta t, \quad k = 1, 2,$$

where $\vec{N}_1$ and $\vec{N}_2$ are normal vectors at Z_1^n and Z_2^n respectively.

The heavy fluid is continuous across the bubble edge and the light fluid is continuous across the spike edge. The continuous phase states on the front are updated by interpolation from interior states after the interior update. Here we describe the update of vanishing phase on the front by applying the method of characteristics and the buoyancy-drag law.

First we update the normal component of the vanishing phase velocity $(v_k^N)_{0k}$ on the edge k by finite differencing (8) and noting that $(v_k^N)_{0k}$ is same as the edge normal velocity $\dot{Z}_k(t) = V_k(t)$:

$$(v_k^N)_{0k}^{n+1} = (v_k^N)_{0k}^n + (-1)^k \Delta t \left\{ A_{0k}^n g - C_k^d \left[\frac{(\rho_k')_{0k}^n}{(\rho_2)_{0k}^n + (\rho_1)_{0k}^n} \right] \frac{(v_k^N)_{0k}^n (v_k^N)_{0k}^n}{(Z_k)^n} \right\} ,$$

where A_{0k}^n is the instantaneous Atwood ratio at edge k, $A_{0k}^n = \frac{(\rho_2)_{0k}^n - (\rho_1)_{0k}^n}{(\rho_2)_{0k}^n + (\rho_1)_{0k}^n}$. For the tangential velocity update, we have

$$(v_k^T)_{0k}^{n+1} = (v_k^T)_{0k}^n$$

due to Eq. (14).

Secondly, we use characteristic differencing to update the pressure at the bubble edge ($k = 1$) by tracing back the C_1^- characteristic from the space-time position (Z_1^{n+1}, t_{n+1}) to (z', t_n), with $z' = Z_1^{n+1} - (v_1^N - c_1)_{01}^n \Delta t \vec{N}_1$. Note z' is located inside the mixing zone. Let $(U_1)'$ be the phase 1 state at this space-time position (z', t_n), found by interpolation on the numerical solution at time t_n. Approximating (15) by finite differences, we have

$$(p_1)_{01}^{n+1} = p_1' + (\xi_1^-)' \beta_1' + (\rho_1 c_1)' \{ (v_1^N)_{01}^{n+1} - (v_1^N)' - g\Delta t \} .$$

At the spike edge ($k = 2$), we similarly obtain an approximation to (15) by tracing back the C_2^+ characteristic from (z_2^{n+1}, t_{n+1}) to (z', t_n) with $z' = Z_2^{n+1} - (v_2^N + c_2)_{02}^n \Delta t \vec{N}_2$:

$$(p_2)_{02}^{n+1} = p_2' + (\xi_2^+)' \beta_2' - (\rho_2 c_2)' \{ (v_2^N)_{02}^{n+1} - (v_2^N)' - g\Delta t \} .$$

Finally we approximate (13) and obtain $(\rho_k)_{0k}^{n+1}$ by noting $(\beta_k)_{0k}^n = 0$ for all n:

$$(\rho_k)_{0k}^{n+1} = (\rho_k)_{0k}^n + \frac{(p_k)_{0k}^{n+1} - (p_k)_{0k}^n}{(c_k^2)_{0k}^n} \ .$$

Note that there is no equation for the vanishing phase associated with the characteristic equations C_1^+ and C_2^- at the two edges, pointing out of the mixing zone. These equations are replaced by the buoyancy drag equation (8) at each edge, so that total number of equations is preserved.

2.2 Tangential Sweep

Once front points have been processed using the normal point propagate operator, a second sweep is performed to incorporate tangential flow information. This is accomplished by projecting the states on a tracked wave near a point onto the tangent plane at the point being updated. As shown in Fig. 1 for two space dimensions, states sl_i and sr_i are evaluated by interpolating points at distances Δs in arclength along the curve, each taken from its respective side of the curve. The tangential projection of these states are then used as data for a standard finite difference solver that provides the final time updated state at the front point. The equations during the tangential sweep are given by

$$\begin{aligned}
\partial_t \beta_k &= -v_T^* \frac{\partial \beta_k}{\partial T} \ , \\
\partial_t \rho_k + \frac{\partial \rho_k v_k^T}{\partial T} &= -\rho_k \frac{(v_k^T - v_T^*)}{\beta_k} \frac{\partial \beta_k}{\partial T} \ , \\
\partial_t (\rho_k v_k^T) + \frac{\partial}{\partial T}(\rho_k v_k^T v_k^T) + \frac{\partial p_k}{\partial T} &= -\rho_k v_k^T \frac{(v_k^T - v_T^*)}{\beta_k} \frac{\partial \beta_k}{\partial T} \\
&\quad - \frac{(p_k - p^*)}{\beta_k} \frac{\partial \beta_k}{\partial T} + \rho_k g_T \ , \\
\partial_t (\rho_k v_k^N) + \frac{\partial}{\partial T}(\rho_k v_k^N v_k^T) &= -\rho_k v_k^N \frac{(v_k^T - v_T^*)}{\beta_k} \frac{\partial \beta_k}{\partial T} \ , \\
\partial_t (\rho_k e_k) + \frac{\partial}{\partial T}(\rho_k e_k v_k^T) + \frac{\partial}{\partial T}(p_k v_k^T) &= -\rho_k e_k \frac{(v_k^T - v_T^*)}{\beta_k} \frac{\partial \beta_k}{\partial T} \\
&\quad + \frac{((p v_T)^* + p^* v_k^T - 2 p_k v_k^T)}{\beta_k} \frac{\partial \beta_k}{\partial T} \\
&\quad + \rho_k v_k^T g_T \ .
\end{aligned} \tag{19}$$

The above equations are the projection of the system (1) onto the tangential direction $\vec{T}$ of the front.

2.3 Interior Update

Our approach to update the states in the interior region is to use the dimensional splitting method by decomposing the equations of motion into x and y components, and then to apply standard finite difference methods in each directional component. For example, our current implementation includes the Lax-Wendroff method [37, 40] and the MUSCL scheme [11, 2] in the x and y direction.

The convergence of the splitting method is given by Crandall and Majda [12]. Strang [42] pointed out that the accuracy of splitting methods is second order if the order in which the one-dimensional problems is solved is alternated, as in $xyyxxy\cdots$.

To couple the front information to the interior states, we consider the irregular finite difference stencils, which overlap, or cross the tracked front. In updating such mesh blocks, we treat the tracked front as an internal time dependent "boundary". Missing stencil points on the "wrong" side of the interface are filled in by extrapolation as a ghost cell [25], using data from the same side of the interface as the mesh block being updated. The ghost cell method was introduced by Glimm, Marchesin and McBryan in 1980 for this purpose. Therefore the front divides the domain into several subdomains. We solve the problem inside each subdomain with front states (from the correct front side) as boundary conditions. In that way, our finite differencing is never performed across the front, and the flow gradient remains perfectly sharp at the front.

3 Incompressible Solutions

In this section we present an analytic solution for the incompressible pressure equations in the one dimensional case, which we use for the validation study in §4. This solution, of independent interest, completes the incompressible solution discussed in [6]. We also present an integral constraint on the incompressible pressures first derived in [33], which insure their equality to the second term in the expansion of the compressible pressures in the incompressible limit. We emphasize the remarkable fact that the incompressible

pressures, in the absence of a compressible limiting flow, are not unique. They are uniquely specified by certain details of the compressible flows from which they are derived as a limit.

3.1 Closed Form Incompressible Pressures

The solutions for the incompressible pressures described in this section depend on earlier analytic solutions for the volume fractions and the velocities [6, 28]. These solutions for β_k and v_k are based on the observation that when the history of the mixing zone edges $Z_k(t)$ are known a priori, then the interface and continuity equations decouple from the momentum equations. This closed form solution for β_k and v_k is summarized in the following theorem.

Theorem 1 *Consider incompressible flows in a finite but large interval $\mathcal{D}$ satisfying the closure models (2) and (5). Assume the boundary condition that the light velocity vanishes at the upper boundary of $\mathcal{D}$. Suppose that both edges $Z_k(t)$ are known and satisfy $V_k \equiv (-1)^k \dot{Z}_k \geq 0$. Suppose that β_k is piecewise C^1 and initial profile $\beta_k(z,0)$ is an invertible function of height z, and that v_k is continuous across the mixing zone edge $Z_{k'}$. Then the interface and continuity equations in (1) have a unique solution for β_k and v_k. The velocity is given as a function of β_k by*

$$v_k = \dot{Z}_k \mu^v_{k'}(\beta_k, t) = \beta_{k'} \dot{Z}_k \frac{V_{k'}}{\overline{V}} \ , \tag{20}$$

where $\overline{V} = \beta_1 V_1 + \beta_2 V_2$. The constitutive law d^v_k in the model (5) is given by

$$d^v_k(t) = \frac{V_{k'}(t)}{V_k(t)} \ . \tag{21}$$

The volume fraction β_k is given by the functional inverse of

$$z(\beta_k, t) = z_0(\beta_k) + \int_0^t v^*(\beta_k, s)\, ds \ , \tag{22}$$

where $z_0(\beta_k)$ is the inverse of the initial volume fraction profile $\beta_k(z,0)$.

Still under the assumptions of Theorem 1, we now describe analytic solutions for the pressures using β_k and t as the independent variables. We

rewrite the momentum equation in (1) as

$$\frac{\partial p_k}{\partial z} + (-1)^k \frac{p^* - p_k}{\beta_k} \frac{\partial \beta_1}{\partial z} = h_k(z,t)\,, \tag{23}$$

where

$$h_k(z,t) = \rho_k \left(g - \frac{D_k v_k}{Dt} \right) . \tag{24}$$

For any quantity q, set

$$\overline{q} \equiv \beta_1 q_1 + \beta_2 q_2\,, \quad \widetilde{q} \equiv q_1 - d_2^p q_2\,, \quad \Delta q \equiv q_1 - q_2\,.$$

The linear combinations $\overline{p}$ and $\widetilde{p}$ decouple the momentum equations into a pair of ordinary differential equations.

$$\frac{\partial \overline{p}}{\partial z} = \overline{h}\,. \qquad \frac{\partial \widetilde{p}}{\partial z} = \widetilde{h}\,. \tag{25}$$

This system can be integrated in closed form in terms of the history of the edge motions.

We begin by writing h_k explicitly as a function of β_k and $\dot{Z}_k$ and its derivatives. With (20) one can verify that

$$\frac{\partial v_k}{\partial \beta_k} = (-1)^{k'} \frac{V_k^2 V_{k'}}{\overline{V}^2} \quad , \quad \frac{\partial v_k}{\partial V_k} = (-1)^k \frac{V_{k'}^2}{\overline{V}^2} \beta_{k'}^2 \quad , \quad \frac{\partial v_k}{\partial V_{k'}} = (-1)^k \frac{V_k^2}{\overline{V}^2} \beta_{k'} \beta_k\,. \tag{26}$$

The h_k terms in (25) contain convective derivatives that can be written in terms of V_k and β_k. Let

$$\zeta_k \equiv (-1)^k \ddot{Z}_k \frac{\partial v_k}{\partial V_k} + (-1)^{k'} \ddot{Z}_{k'} \frac{\partial v_k}{\partial V_{k'}} = \frac{\beta_{k'}}{\overline{V}^2} (\ddot{Z}_k V_{k'}^2 \beta_{k'} - \ddot{Z}_{k'} V_k^2 \beta_k)\,. \tag{27}$$

Then

$$\begin{aligned} \frac{\partial v_k}{\partial t} &= (-1)^k \frac{\partial v_k}{\partial V_k} \ddot{Z}_k + (-1)^{k'} \frac{\partial v_k}{\partial V_{k'}} \ddot{Z}_{k'} + \frac{\partial v_k}{\partial \beta_k} \frac{\partial \beta_k}{\partial t} \\ &= \zeta_k - \frac{\partial v_k}{\partial \beta_k} \frac{\partial (\beta_k v_k)}{\partial z} \\ &= \zeta_k - \frac{\partial v_k}{\partial \beta_k} \left(v_k + \beta_k \frac{\partial v_k}{\partial \beta_k} \right) \frac{\partial \beta_k}{\partial z}\,. \end{aligned}$$

Substituting this result into h_k and using (26), we obtain

$$\begin{aligned} h_k &= \rho_k g - \rho_k \zeta_k + \rho_k \left(\frac{\partial v_k}{\partial \beta_k} (v_k + \beta_k \frac{\partial v_k}{\partial \beta_k}) \frac{\partial \beta_k}{\partial z} - v_k \frac{\partial v_k}{\partial \beta_k} \frac{\partial \beta_k}{\partial z} \right) \\ &= \rho_k g - \rho_k \zeta_k + \rho_k \beta_k \left(\frac{\partial v_k}{\partial \beta_k} \right)^2 \frac{\partial \beta_k}{\partial z} \\ &= \rho_k g - \rho_k \zeta_k + \rho_k \beta_k \frac{V_k^4 V_{k'}^2}{\overline{V}^4} \frac{\partial \beta_k}{\partial z} . \end{aligned}$$

Therefore, the right side of (25) is given explicitly as a function of β_k,

$$\begin{aligned} \overline{h} &= \overline{\rho} g + \frac{V_1^2 V_2^2}{\overline{V}^4} \left(\beta_1^2 \rho_1 V_1^2 - \beta_2^2 \rho_2 V_2^2 \right) \frac{\partial \beta_1}{\partial z} + \\ &\qquad (\rho_1 - \rho_2) \frac{\beta_1 \beta_2}{\overline{V}^2} \left(\ddot{Z}_2 V_1^2 \beta_1 - \ddot{Z}_1 V_2^2 \beta_2 \right) , \\ \widetilde{h} &= \widetilde{\rho} g + \frac{V_1^2 V_2^2}{\overline{V}^4} \left(\beta_1 \rho_1 V_1^2 + \beta_2 \rho_2 d_2^p V_2^2 \right) \frac{\partial \beta_1}{\partial z} + \\ &\qquad \frac{1}{\overline{V}^2} (\rho_1 \beta_2 + d_2^p \rho_2 \beta_1) \left(\ddot{Z}_2 V_1^2 \beta_1 - \ddot{Z}_1 V_2^2 \beta_2 \right) . \end{aligned} \tag{28}$$

Observe that $\widetilde{\rho} = 0$ if $d_2^p = \rho_1 / \rho_2$, so that in this case $\widetilde{h}$ is independent of g.

The system (25) may be integrated with respect to z since β_k is a function of z. Instead, we rewrite the system in terms of β_1 since β_1 is expressed as an invertible function of z. We now transform these integrals into β_1 integrals. We differentiate $v^* = \mu_2^v v_1 + \mu_1^v v_2$ with respect to β_k using (20) to obtain

$$\frac{\partial v^*}{\partial \beta_k} = 2(-1)^{k'} \frac{\dot{V}_{k'}^2 V_k^2}{\overline{V}^3} . \tag{29}$$

This result is inserted into the derivative of (22) with respect to β_k. If we assume an infinitesimally thin initial mixing zone, then the term $z_k'(\beta_k) = dz_0 / d\beta_k$ in (22) vanishes and we obtain

$$\frac{\partial z}{\partial \beta_k} = (-1)^{k'} 2 \int_0^t \frac{V_1^2(s) V_2^2(s)}{\overline{V}^3(s)} ds . \tag{30}$$

This identity reduces the integrals in z to integrals in β_1.

3.1.1 Weakly Self Similar Solutions

Incompressible solutions that correspond to edge position functions of the form $Z_k(t) = (-1)^k \alpha_k Z(t)$ are called *weakly self-similar*. Define $V(t) = \dot{Z}(t)$.

The weak self similar hypothesis allows evaluation of (30) as

$$\frac{\partial z}{\partial \beta_k} = (-1)^{k'} 2 \frac{\alpha_1^2 \alpha_2^2}{\overline{\alpha}^3} \left(\int_0^t V(s) ds \right) = (-1)^{k'} 2 \frac{\alpha_1^2 \alpha_2^2}{\overline{\alpha}^3} Z(t) \quad , \tag{31}$$

assuming $Z(0) = 0$. As a result, the integral of (25) can be written as an integral with respect to β_k. The integrand is a rational function of β_k with a denominator which is a power of a linear function of β_k times a polynomial in the instantaneous scale factor $Z(t)$ and its first and second derivatives. These integrals can be evaluated explicitly by a partial fraction decomposition, leading to the weakly self-similar pressure solutions

$$\begin{aligned}
\overline{p}(\beta_1, t) &= p_2(Z_1) + \beta_1 g Z(t) A_0 + \beta_1 V^2(t) B_0 + \beta_1 \Delta\rho \, \dot{V}(t) Z(t) C_0 \ , \\
A_0 &= \frac{\alpha_1^2}{\overline{\alpha}^2} (\rho_2 \overline{\alpha} + \overline{\rho} \alpha_2) \ , \\
B_0 &= \frac{\alpha_1^2 \alpha_2}{3\overline{\alpha}^3} \left[\beta_1^2 \Delta\rho \ \alpha_1^2 - 3\beta_2 \rho_2 \alpha_2 \overline{\alpha} \right] \ , \\
C_0 &= \frac{\alpha_1^3 \alpha_2}{3\overline{\alpha}^3 (\Delta\alpha)^2} \left[-2\alpha_1 (\overline{\alpha}^2 + \overline{\alpha}\alpha_2 + \alpha_2^2) + 3\overline{\alpha}(\alpha_1 + \alpha_2)(\alpha_2 + \overline{\alpha}) - 6\alpha_2 \overline{\alpha}^2 \right] \ , \\
\widetilde{p}(\beta_1, t) &= \widetilde{p}(Z_1) + \beta_1 g \widetilde{\rho} Z(t) D_0 + \beta_1 V^2(t) E_0 + \beta_1 \dot{V}(t) Z(t) F_0 \ , \\
D_0 &= \frac{\alpha_1^2}{\overline{\alpha}^2} (\alpha_2 + \overline{\alpha}) \ , \\
E_0 &= \frac{\alpha_1^2}{6\overline{\alpha}^3 \Delta\alpha} [-2\alpha_1 \widetilde{\rho\alpha} (\alpha_2^2 + \alpha_2 \overline{\alpha} + \overline{\alpha}^2) + 3\overline{\alpha} \widetilde{\rho\alpha^2} (\alpha_2 + \overline{\alpha})] \ , \\
F_0 &= \frac{\alpha_1^3}{3\overline{\alpha}^3 \Delta\alpha} \left[2\widetilde{\rho\alpha} (\alpha_2^2 + \alpha_2 \overline{\alpha} + \overline{\alpha}^2) - 3\alpha_2 \overline{\alpha} \widetilde{\rho} (\alpha_2 + \overline{\alpha}) \right] \ .
\end{aligned} \tag{32}$$

We recognize the A_0 and D_0 terms as buoyancy terms as they are multiplied by gravity. Similarly, the B_0 and E_0 terms, both proportional to V^2 are drag terms, while the C_0 and F_0 terms, proportional to $\ddot{Z}$, are inertial terms. The constitutive law closure (7) implies $\widetilde{\rho} = 0$, so that the buoyancy contribution to $\widetilde{p}$ vanishes.

3.1.2 The General Incompressible Pressure Solution

In the general the identity (31) is not valid. Since the history integrals originating in (30) cannot be evaluated in closed form, they appear in the final expression for the pressures. We reverse the order of integration between β_1 and t. For fixed time s in the history integral, the β_k integrals are again evaluated in closed form by a partial fraction decomposition.

The analytic solutions for $\overline{p}$ and $\widetilde{p}$ are found by integrating these expressions. We concentrate on the solution for $\overline{p}$. Integrating the first equation of (28), we have

$$\begin{aligned}
\overline{p}(z) &= \beta_1 p_1(z) + \beta_2 p_2(z) = \overline{p}(Z_1) + \int_{Z_1}^{z} \overline{h} dz \\
&= p_2(Z_1) + 2g \int_0^t V_1^2(s) V_2^2(s) \left[\int_0^{\beta_1} \frac{\rho_1 \phi_1 + \rho_2 \phi_2}{\overline{V}^3(s)} d\phi_1 \right] ds \\
&+ V_1^2(t) V_2^2(t) \int_0^{\beta_1} \frac{\rho_1 V_1^2(t) \phi_1^2 - \rho_2 V_2^2(t) \phi_2^2}{\overline{V}^4(t)} d\phi_1 \\
&+ 2(\rho_2 - \rho_1) \int_0^t V_1^2(s) V_2^2(s) \\
&\times \left[\int_0^{\beta_1} \frac{\phi_1 \phi_2}{\overline{V}^3(s) \overline{V}^2(t)} \left(\ddot{Z}_1 V_2^2(t) \phi_2 - \ddot{Z}_2 V_1^2(t) \phi_1 \right) d\phi_1 \right] ds \, .
\end{aligned} \tag{33}$$

Note that all accelerations $\ddot{Z}_k = \ddot{Z}_k(t)$ are functions of time t and that $\phi_1 + \phi_2 = 1$. Analytic solutions can be obtained since the denominator involves only powers of $\overline{V}(s)$ and $\overline{V}(t)$, which are linear functions of β_k. We omit details concerning the integrations and partial fraction decompositions. All identities were found with the assistance of the computer algebra program Maple.

It is simple to check that

$$\int_0^{\beta_1} \frac{\rho_1 \phi_1 + \rho_2 \phi_2}{\overline{V}^3(s)} \, d\phi_1 = \frac{1}{2} \frac{\beta_1}{V_2^2(s) \overline{V}^2(s)} (\rho_2 \overline{V}(s) + \bar{\rho} V_2(s)) \, . \tag{34}$$

Similarly for the second term, the integration with respect to β_1 is performed.

$$\int_0^{\beta_1} \frac{1}{\overline{V}^4(t)}(\rho_1 V_1^2(t)\phi_1^2 - \rho_2 V_2^2(t)\phi_2^2)d\phi_1 = \frac{1}{3}\frac{\beta_1}{V_2(t)\overline{V}^3(t)}\left(\beta_1^2\Delta\rho\, V_1^2(t) - 3\beta_2\rho_2 V_2(t)\overline{V}(t)\right) . \tag{35}$$

The partial fraction decomposition for the last integrand in (33) gives rise to four different rational functions. We factor out the terms involving $\ddot{Z}_k$. Let $\eta = V_2(t)V_1(s) - V_1(t)V_2(s)$.

$$\begin{aligned}
&\int_0^{\beta_1} \frac{\phi_1\phi_2}{\overline{V}^3(s)\overline{V}^2(t)}\left(\ddot{Z}_1 V_2^2(t)\phi_2 - \ddot{Z}_2 V_1^2(t)\phi_1\right) d\phi_1 = \\
&-\frac{1}{\eta^4}(V_2^3(t)\ddot{Z}_1 + V_1^3(t)\ddot{Z}_2) \times \\
&\left((V_2(t)V_1(s) + V_1(t)V_2(s))\ln\left(\frac{\overline{V}(t)V_2(s)}{\overline{V}(s)V_2(t)}\right) + \beta_1\eta(\frac{V_1(t)}{\overline{V}(t)} + \frac{V_1(s)}{\overline{V}(s)})\right) \\
&-\frac{1}{\eta^4}(V_2^2(t)V_2(s)\ddot{Z}_1 + V_1^2(t)V_1(s)\ddot{Z}_2)\left(V_1(t)V_2(t)\ln\left(\frac{\overline{V}(t)V_2(s)}{\overline{V}(s)V_2(t)}\right)\right. \\
&\left.-\frac{\beta_1 V_1(s)\eta^2(V_2(s) + \overline{V}(s))}{2V_2(s)\overline{V}^2(s)\Delta V(s)} + \frac{\beta_1\eta(V_2(t)V_1^2(s) - V_1(t)V_2^2(s))}{V_2(s)\overline{V}(s)\Delta V(s)}\right) .
\end{aligned} \tag{36}$$

When these expressions are substituted into (33) we obtain

$$\overline{p}(z) = p_2(Z_1) + \int_{Z_1}^{z} \overline{h}\, dz = p_2(Z_1) + \beta_1 g A + \beta_1\overline{V}^2(t)B + 2\Delta\rho C \quad , \tag{37}$$

where

$$\begin{aligned}
A &= \int_0^t \frac{V_1^2(s)}{\overline{V}^2(s)}(\rho_2\overline{V}(s) + \overline{\rho}V_2(s))ds \ , \\
B &= \frac{V_1^2(t)V_2(t)}{3\overline{V}^5(t)}\left(\beta_1^2\Delta\rho\, V_1^2(t) - 3\beta_2\rho_2 V_2(t)\overline{V}(t)\right) \ , \\
C &= \int_0^t \frac{V_1^2(s)V_2^2(s)}{\eta^4}\Bigg[(V_2^3(t)\ddot{Z}_1(t) + V_1^3(t)\ddot{Z}_2(t))\times
\end{aligned}$$

$$\left((V_2(t)V_1(s)+V_1(t)V_2(s))\ln\left(\frac{\overline{V}(t)V_2(s)}{\overline{V}(s)V_2(t)}\right)+\beta_1\eta(\frac{V_1(t)}{\overline{V}(t)}+\frac{V_1(s)}{\overline{V}(s)})\right)$$
$$+(V_2^2(t)V_2(s)\ddot{Z}_1(t)+V_1^2(t)V_1(s)\ddot{Z}_2(t))\left(V_1(t)V_2(t)\ln\left(\frac{\overline{V}(t)V_2(s)}{\overline{V}(s)V_2(t)}\right)\right.$$
$$\left.-\frac{\beta_1V_1(s)\eta^2(V_2(s)+\overline{V}(s))}{2V_2(s)\overline{V}^2(s)\Delta V(s)}+\frac{\beta_1\eta(V_2(t)V_1^2(s)-V_1(t)V_2^2(s))}{V_2(s)\overline{V}(s)\Delta V(s)}\right)\Bigg]ds\,.$$

A similar analysis for $\widetilde{p}$ (details omitted) leads to:

$$\widetilde{p}(z)=\widetilde{p}(Z_1)+\int_{Z_1}^{z}\widetilde{h}\;dz=\widetilde{p}(Z_1)+\beta_1g\widetilde{\rho}D+\beta_1E+2F\;, \tag{38}$$

where

$$\begin{aligned}
D &= \int_0^t\frac{V_1^2(s)}{\overline{V}^2(s)}(V_2(s)+\overline{V}(s))ds\;,\\
E &= \frac{V_1^2(t)}{6\overline{V}^3(t)\Delta V(t)}\times\\
&\quad\left(-2\widetilde{\rho V}(t)V_1(t)\left(V_2^2(t)+V_2(t)\overline{V}(t)+\overline{V}^2(t)\right)+3\widetilde{\rho V^2}(t)\overline{V}(t)(V_2(t)+\overline{V}(t))\right)\;,\\
F &= \int_0^t\frac{V_1^2(s)V_2^2(s)}{\eta^4}\Bigg[\left(V_2(s)V_1^2(t)\ddot{Z}_2(t)+V_1(s)V_2^2(t)\ddot{Z}_1(t)\right)\times
\end{aligned}$$

$$\left(2\widetilde{\rho V}(t)\Delta V(t)\ln\left(\frac{\overline{V}(t)V_2(s)}{\overline{V}(s)V_2(t)}\right)+\frac{\beta_1\eta^2}{V_2(s)\overline{V}(s)}\left\{\frac{\widetilde{\rho V}(t)\Delta V(s)}{\eta}-\frac{\widetilde{\rho V}(s)(V_2(s)+\overline{V}(s))}{2V_2(s)\overline{V}(s)}\right\}\right)$$
$$+\left(V_1(t)\ddot{Z}_2(t)+V_2(t)\ddot{Z}_1(t)\right)\times$$
$$\left(2\widetilde{\rho V^2}(t)\eta\ln\left(\frac{\overline{V}(t)V_2(s)}{\overline{V}(s)V_2(t)}\right)+\beta_1V_1(t)V_2(t)\eta\left\{\frac{\widetilde{\rho V}(t)\Delta V(t)}{V_2(t)\overline{V}(t)}+\frac{\widetilde{\rho V}(s)\Delta V(s)}{V_2(s)\overline{V}(s)}\right\}\right)$$
$$+\left(V_1(s)\ddot{Z}_2(t)+V_2(s)\ddot{Z}_1(t)\right)\widetilde{\rho V}(t)V_1(t)V_2(t)\Delta V(t)\ln\left(\frac{\overline{V}(t)V_2(s)}{\overline{V}(s)V_2(t)}\right)\Bigg]ds\;\;.$$

Again we recognize A and D as buoyancy terms, B and E as drag and C and F as inertial terms. The parallelism of structure between the A_0 and A *etc.* terms is evident. The buoyancy term $\beta_1g\widetilde{\rho}D$ vanishes due to (7). Observe that the $\overline{p}$ and $\widetilde{p}$ drag terms are instantaneous, *i.e.* have no history integral, while the buoyancy and inertial terms require history integrals.

3.2 Unique Solvability of the Pressure Equation

The system (25) requires two independent boundary conditions. Assuming continuity of the pure to mixed fluid pressures, we have $\overline{p}(Z_1) = p_2(Z_1)$ and $\overline{p}(Z_2) = p_1(Z_2)$. However, these two values are are not independent, as they are related by the identity

$$\overline{p}(Z_2) = \overline{p}(Z_1) + \int_{Z_1}^{Z_2} (\beta_1 h_1 + \beta_2 h_2) dz = \overline{p}(Z_1) + \int_{Z_1}^{Z_2} \overline{h} dz \,,$$

and so an additional condition is needed. This new relation is obtained by taking the incompressible limit of the compressible equations. The physical meaning of the incompressible pressure is quite different from that of the compressible case. Assume that the two compressible fluids are described by polytropic equations of state,

$$p_k = \lambda^2 A_k \rho_k^{\gamma_k} \,. \tag{39}$$

The entropy of fluid k is given by $A_{k,\lambda} = \lambda^2 A_k$. The incompressible limit is obtained as $\lambda \to \infty$. In this section, we assume isentropic flow, so that the A_k are constant.

By [33], the state variables and constitutive parameters admit an expansion of the form

$$\begin{aligned}
\beta_k &= \beta_k^\infty + O(\lambda^{-1}) \,, \\
v_k &= v_k^\infty + O(\lambda^{-1}) \,, \\
\rho_k &= \rho_k^\infty + O(\lambda^{-2}) \,, \\
p_k &= \lambda^2 p_k^0 + p_k^\infty + O(\lambda^{-1}) \,, \\
d_k^v &= d_k^{v\infty} + \lambda^{-1} d_k^{v(1,s)} + \lambda^{-2} d_k^{v(2,s)} + O(\lambda^{-3}) \,,
\end{aligned} \tag{40}$$

where the superscript ∞ indicates the incompressible solution and the exponent (j, s), $j = 1, 2$, indicates the jth order term for the slow variables in the expansion. Here $\lambda^2 a_k^2 = c_k^2(\rho_k^\infty) = \lambda^2 A_k \gamma_k \rho_k^{\infty \gamma_k - 1}$ is the leading order term for the sound speed squared in fluid k.

Note the quadratic leading order term in powers of λ in the pressure. This term equals the pressure defined by the equation of state for fluid k, evaluated at ρ_k^∞. Thus, $p_k^0 = A_k (\rho_k^\infty)^{\gamma_k}$. Continuity of the compressible pressures at the interface requires $\lambda^2 A_1 (\rho_1^\infty)^{\gamma_1} = \lambda^2 A_2 (\rho_2^\infty)^{\gamma_2}$ and therefore,

$$A_2 = \frac{(\rho_1^\infty)^{\gamma_1}}{(\rho_2^\infty)^{\gamma_2}} A_1 \,. \tag{41}$$

For incompressible flow, Theorem 1 gives the closure relation (21). Asymptotic analysis for slightly compressible flows shows that the relation (6) provides the equations

$$d_1^{v(1,s)}(t) = \left(\frac{V_2}{V_1}\right)^{(1,s)} = \frac{V_1^\infty V_2^{(1,s)} - V_2^\infty V_1^{(1,s)}}{V_1^{\infty\,2}}\,, \tag{42}$$

$$\begin{aligned} d_1^{v(2,s)}(t) &= \left(\frac{\displaystyle\int_{Z_1}^{Z_2} \frac{\partial v_2}{\partial z} + \frac{1}{\rho_2}\frac{D_2\rho_2}{Dt}\,dz}{\displaystyle\int_{Z_1}^{Z_2} \frac{\partial v_1}{\partial z} + \frac{1}{\rho_1}\frac{D_1\rho_1}{Dt}\,dz}\right)^{(2,s)} \\ &= \frac{-d_1^{v(1,s)}V_1^{(1,s)} - d_1^{v\infty}V_1^{(2,s)} + V_2^{(2,s)}}{V_1^\infty} \\ &\quad - \frac{1}{V_1^\infty}\left\{\int_{Z_1^\infty}^{z^{+\infty}} \frac{\beta_1^\infty + d_1^{v\infty}}{\rho_1^\infty a_1^2}\left(\frac{\partial p_1^\infty}{\partial t} + v_1^\infty\frac{\partial p_1^\infty}{\partial z}\right)dz \right. \\ &\quad \left. + \int_{z^{-\infty}}^{Z_2^\infty} \frac{\beta_2^\infty - 1}{\rho_2^\infty a_2^2}\left(\frac{\partial p_2^\infty}{\partial t} + v_2^\infty\frac{\partial p_2^\infty}{\partial z}\right)dz\right\} \end{aligned} \tag{43}$$

for the constitutive law d_k^v through second order in the Mach number. Here $V_k^{(j,s)} = |\dot{Z}_k^{(j,s)}(t)|$, $Z_k^{(j,s)} = Z_k^{(j,s)}(t)$ is the j-th order term in the expansion of the compressible mixing zone edge Z_k, and $z = z^{+\infty}$ ($z = z^{-\infty}$) is defined as the position of the upper (lower) wall of $\mathcal{D}$. Specifically, Eq. (43) resolves a degree of freedom in the incompressible pressures related to the relative compressibility of the two fluids. The incompressible pressures are uniquely determined by the limiting sound speeds a_k of the two phases and the volume creation constitutive law d_1^v in the weakly compressible $(2, s)$ limit. These relations and the convergence of the compressible multiphase solution to the incompressible solutions are studied in [33].

4 Simulation Studies

Our numerical studies aim to validate the algorithm described in §2 and explore the relationship between the model for edge motion (8) and our multiphase model inside the mixing zone. Both experiments are performed near the incompressible limit and therefore depend on the analysis of the compressible equations in the incompressible limit [33] and on the analytic solutions for this limit, both of which are summarized in §3.

We begin by reviewing the initialization of our model for acceleration driven fluid mixing. The two important parameters controlling the initialization used in §4.1 and §4.2 are the compressibility λ, see (39) and (40), and the drag coefficients C_k in (8). The other parameters are adjusted to produce an initialization for the compressible code with few transients near the incompressible limit $\lambda \to \infty$.

The initialization proceeds as follows. For some dimensionless set of units, assume that the height z of the container is parameterized by the interval $[-1, 1]$. Suppose that the heavy fluid of density $\rho_2^\infty = 0.4$ is located below the light fluid of density $\rho_1^\infty = 0.1$ and that the container is given an upwards acceleration of $g = 0.3$. The Atwood number is therefore $A \equiv (\rho_2^\infty - \rho_1^\infty)/(\rho_1^\infty + \rho_2^\infty) = 0.6$. Each fluid is given a γ-law as an EOS with $\gamma_1 = 1.4$ and $\gamma_2 = 1.8$ for respectively the light and heavy fluid.

According to self-similar edge motions of the incompressible flow,

$$Z_k = (-1)^k \alpha_k A g t^2 \,, \tag{44}$$

there remains only one parameter, the mixing growth rate α_k, for the edges. According to formulas (9) and (10), the growth rates α_k are equivalent to the drag coefficients C_k. When $A \leq 0.9$, the hypothesis of a stationary center of mass [29] for the mixing zone is approximately valid [7]. This hypothesis implies an additional constraint, which determines the ratio

$$\frac{\alpha_2}{\alpha_1} = \frac{-\frac{1}{3}(\rho_2^\infty - \rho_1^\infty) + \sqrt{\frac{1}{9}(\rho_2^\infty - \rho_1^\infty)^2 + 4\rho_1^\infty \rho_2^\infty}}{2\rho_1^\infty} \tag{45}$$

of the mixing growth rates α_k as an exact identity [6] for incompressible flow. At the bubble edge, experimental results [43, 39, 13, 15, 16] indicate that $\alpha_1 \approx 0.06$, and by (45), α_2 is fixed at $\alpha_2 = 0.093693$.

In order to have a reasonable number of grid points initially within th mixing zone, we set $Z_2(t_0) = 0.1$ and begin the experiment at the time

$$t_0 = \sqrt{\frac{Z_2(t_0)}{\alpha_2 A g}} \,,$$

after the beginning of the expansion of the mixing zone. This value t_0 is then used with (45) to obtain the initial position of $Z_1(t_0)$ and the velocities

$\dot{Z}_k(t_0)$, $k = 1, 2$:

$$\begin{aligned} Z_1(t_0) &= -0.06403882\,, \\ \dot{Z}_1(t_0) &= v_1(Z_1(t_0), t_0) = -V_1(t_0) = -0.05259731\,, \\ \dot{Z}_2(t_0) &= v_2(Z_2(t_0), t_0) = V_2(t_0) = 0.08213348\,. \end{aligned} \tag{46}$$

The initial state for compressible multiphase flow $(\beta_k(0), \rho_k(0), v_k(0), p_k(0))$ is defined as

$$\begin{aligned} \beta_k(0) &= \beta_k^\infty(t_0)\ , \\ v_k(0) &= v_k^\infty(t_0)\ , \\ \rho_k(0) &= \rho_k^\infty(t_0)\ , \\ p_k(0) &= \lambda^2 p_k^0 + p_k^\infty(t_0)\ , \end{aligned} \tag{47}$$

according to (40).

4.1 Model Dependence on Edge Motions

The equation

$$\begin{aligned} (-1)^k \rho_k \frac{d^2 Z_k(t)}{dt^2} &= (\rho_2 - \rho_1) g + \frac{\partial (p_1 - p_2)}{\partial z} \\ &\quad - \rho_{k'} V_k^2 \frac{\partial \beta_1}{\partial z} - (-1)^k \left(d_{k'}^p - 1\right)(p_1 - p_2) \frac{\partial \beta_1}{\partial z} \end{aligned} \tag{48}$$

has been derived [28] as an exact consequence of the momentum equation for incompressible flow. Here the RHS of this equation is evaluated along the trajectory $z = Z_k(t)$. Newton's law (48) of acceleration relates the phenomenological drag coefficient and added mass in (8) to the pressure difference and the gradient of the pressure difference. These latter quantities, determined in closed form for incompressible flow in (37)-(38), thus allow a derivation of (8) with a theoretical determination of added mass and drag. The interpretation of the separate terms in (37)-(38) is discussed in §3.1. The structure of these terms is complicated, and a simple interpretation of the connection between (48), (8) and (37)-(38) is outside the scope of the present work. However, we make a few qualitative observations, based on the numerical solution of the chunk mix multiphase equations (1).

In (48) the acceleration term is positive for both $k = 1$ and $k = 2$. The gravity term $(\rho_2 - \rho_1)g$ is positive and thus increases acceleration, while the

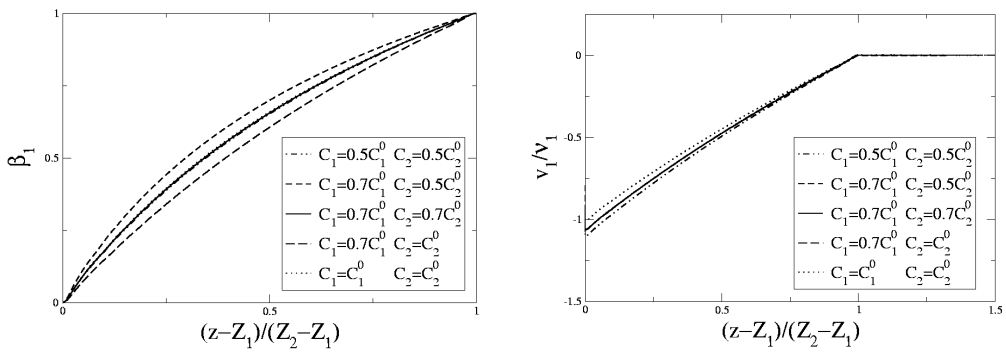

Figure 2: The insensitivity of the volume fraction and scaled velocity to the drag coefficients C_k and the resulting mixing zone edges Z_k when $\lambda^2 = 25$ and $t = 3.0$. These variables, when plotted *vs.* a scaled height $(z - Z_1)/(Z_2 - Z_1)$, are nearly indistinguishable for a considerable variation in the Z_k. Here C_k^0 is the incompressible drag coefficient.

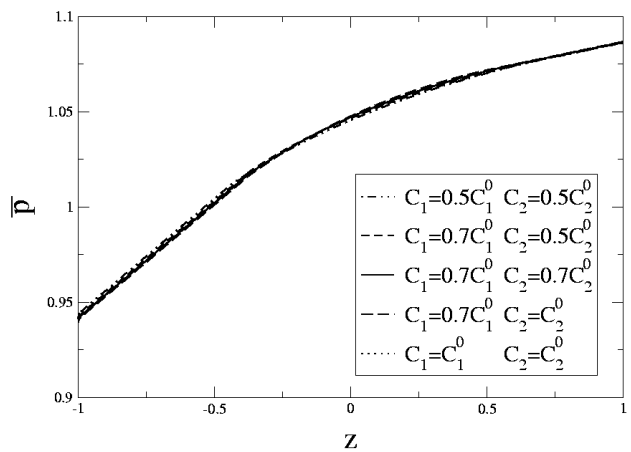

Figure 3: Insensitivity of the mean pressure $\overline{p}$ to variation of the drag coefficients and the resulting edge motions Z_k. Here $\overline{p}$ is plotted *vs.* z and the other parameters are as in Fig. 2.

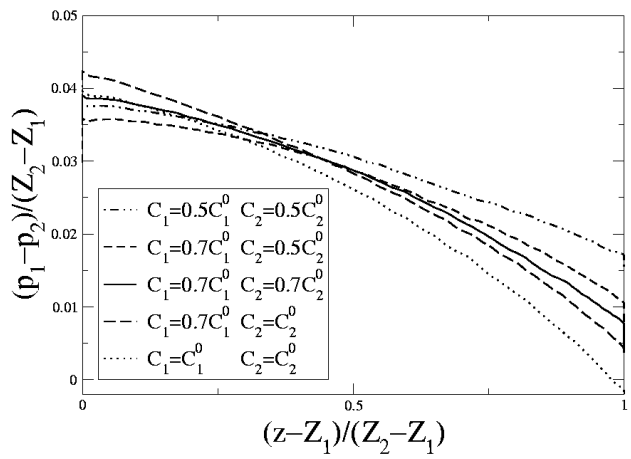

Figure 4: The sensitivity of the pressure difference for the compressible equations to the drag coefficients and resulting mixing zone edges Z_k when $\lambda^2 = 25$ and $t = 3.0$. We plot $(p_1 - p_2)/(Z_2 - Z_1)$ *vs.* $(z - Z_1)/(Z_2 - Z_1)$ for several choices of drag coefficients C_k and corresponding growth rate coefficients $\alpha_k = \alpha_k(C_k)$.

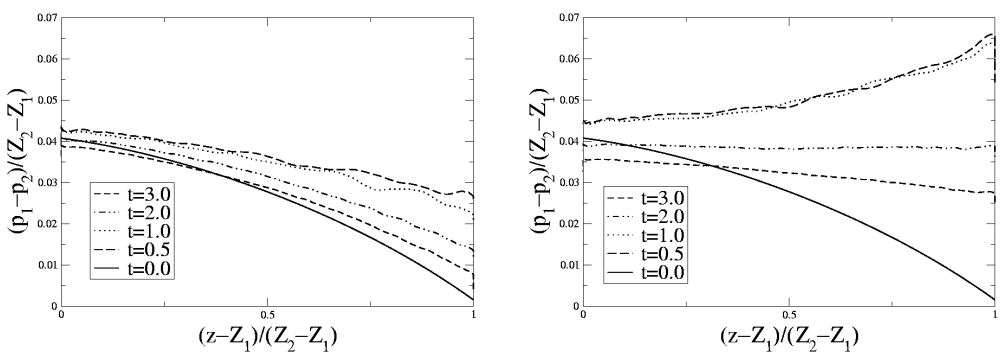

Figure 5: The pressure difference depends on time. Displayed are the pressure difference curves for $t = 0.0,\ 0.5,\ 1.0,\ 2.0,\ 3.0$. Left: $\lambda^2 = 25$ (nearly incompressible), Right: $\lambda^2 = 5$ (moderately compressible).

drag term proportional to $-V_k^2$, being negative, always decelerates. Assuming $d_k^p = \rho_{k'}/\rho_k$, the coefficient $-(-1)^k(d_{k'}^p - 1)\partial\beta_1/\partial z$ of the pressure difference is always nonpositive. Since $p_1 - p_2$ is positive in Figs. 4 and 5, this term in (48) is a deceleration term for the fluid parameters considered here. The pressure difference gradient, generally negative for the edge motions shown here, is also a deceleration term.

From the above analysis, we can understand the dependence of the multiphase solution on the edge motions $Z_k(t)$. The Z_k are determined through specification of the drag coefficient C_k. Since the dependence of the C_k on compressibility is not understood, we explore the dependence of the solution on the C_k. The influence of a variation in C_k on the multiphase solutions can most easily understood through its influence on α_k *via* (10). We plot normalized variables with this direct effect removed. Fig. 2 (left) indicates that the quantity β_k plotted in terms of a normalized height variable, is insensitive to changes in the mixing growth rates α_k (determined by the drag coefficient $C_k(t)$). The edge velocity scaling (linear growth in time) is complicated due to an initial time offset in the amount t_0, and by the use of an incompressible initialization for the compressible dynamical evolution. Thus we introduce the scaling velocity

$$\mathcal{V}_k(t) = 2\alpha_k^0 Agt_0 + 2\alpha_k Agt \approx (-1)^k V_k(t) \quad , \tag{49}$$

where $\alpha_k^0 = \alpha_k(C_k^0)$ and $\alpha_k(C_k)$ are defined by (10) and $t \geq 0$. From Fig. 2 (right), we see that $v_k/\mathcal{V}_k$ is insensitive to the choice of compressible drag coefficients. In fact the small remaining dependence on the compressible drag coefficients in Fig. 2 (right) is due to the fact that $V_k(t)/\mathcal{V}_k(t)$ is not exactly equal to $(-1)^k$. See the left edge of Fig 2 (right) where $v_k(Z_k)/\mathcal{V}_k = V_k/\mathcal{V}_k \approx (-1)^k$. A plot of v_k/V_k *vs.* $z/(Z_2 - Z_1)$ (not shown) displays no visible dependence on the drag coefficient. Similarly, $\overline{p}$, plotted *vs.* z in Fig. 3, is insensitive. The variation in the drag coefficient considered here corresponds to 30% and 70% increments in the edge motions (and α's), relative to the incompressible edge motions determined by the incompressible drag coefficients C_k^0.

However, in Fig. 4, the scaled pressure difference and its gradient, especially at the spike edge of the mixing zone, are seen to be sensitive to the drag coefficients and thus to the edge motions they determine. As the edges move faster (*i.e.* as the drag coefficient is decreased), the pressure difference at the spike edge responds with an increase in $(p_1 - p_2)/(Z_2 - Z_1)$ (increased

deceleration) and in $\nabla(p_1 - p_2)$ (decreased deceleration). Thus we see that the modification in the acceleration is accommodated by a change in the balance between the contribution of these two forces. Surprisingly, this balance is sensitive to a change in either the bubble or the spike drag coefficient. Between these two terms at the bubble edge, the gradient term appears to be more significant at the spike edge. At the bubble edge, the gradient of the pressure difference is nearly zero, and the pressure difference induced drag results mainly from the pressure difference term. This term scales directly with the change in edge positions. Thus we see little competition between the two terms, and the one term which plays an active role varies in direct proportion to the effect causing this change. The present discussion applies only to the Atwood number ($A = 0.6$) considered here, and does not fully explore the role of these two pressure difference terms in fixing the value for the phenomenological drag coefficient.

Initialization transients occur in the balance between the two pressure difference terms. After the transients have died out, the pressure difference resembles its incompressible value qualitatively, and this late time pressure difference approaches the analytically determined value in the incompressible limit. See Fig. 5. In the nearly incompressible left frame, about 50 sound wave crossing have occured, and initialization transients are small for the time final time shown, $t = 3.0$. In the more compressible right frame, only about 10 sound speed crossings have occured. Thus there has been less time for the transients to decay in the right frame. Moreover, the incompressible initialization used here will generate larger transients in the more compressible right frame. For single phase Euler equations, it has been proved by the uniform analysis that a more compressible system is more oscillatory in early time and that the oscillatory waves decay after a certain small time [34, 35, 32]. This fact is not guaranteed for the multiphase flow equations. The complete analysis of oscillatory part of solutions for the multiphase flow equations has not been reported yet. In Fig. 5 the $t = 0.5$ and $t = 1.0$ curves of the scaled pressure difference involve initialization transients rather than oscillatory waves.

We recall that the nonuniqueness of the incompressible solution [28] is required to accommodate distinct incompressible limits for the pressure difference. Specifically the incompressible pressure difference depends on the ratios of compressible sound speeds (compressibilities) and compressible corrections to the edge motion $Z_k(t)$. The latter depend on the compressibilities, the hydrostatic temperature stratification, and compressibility corrections to

the buoyancy drag equation (such as a dependence of the drag on the compressibility). For this reason, we believe the explicit dependence on the edge motions will turn out to be a strength, not a weakness of the multiphase equations (1), in allowing the full range of solutions physically achievable.

4.2 Validation

We validate our code *via* convergence under mesh refinement and convergence of the compressible solutions to the incompressible limit given in §3 as $\lambda \to \infty$.

4.2.1 Convergence to the Incompressible Limit

The incompressible limit of the single phase compressible Euler equations has been studied theoretically in higher space dimensions [18, 34, 35]. The multiphase flow case, in contrast, presents additional difficulties, so that even one dimensional multiphase flow is nontrivial. We rely here on the one dimensional multiphase flow analysis with a uniformly valid asymptotic expansion obtained previously [33]. The difference $p_1 - p_2$ between the pressures of the two fluids is the most sensitive of the primitive variables in the equations, as we see when studying convergence in the incompressible limit.

The incompressible limit is difficult to achieve numerically within a compressible computational framework due to the short time steps (large sound speed) and possible oscillatory behavior which are characteristic of compressible simulations. As shown in [33] the solutions generally decompose into a slow expansion part with a slow time scale and an oscillatory part with a fast time scale. The oscillatory component is evidence of rapid equilibration, which complicates the numerical convergence to the incompressible limit. Our use of the incompressible limit solution for initialization reduces the fast time scale oscillations. While fast variable oscillations are of interest, we have largely eliminated them from simulations presented in this paper.

In studying the limit $\lambda \to \infty$, we set $C_k = C_k^0$ for $\lambda^2 = 100$, $C_k = 0.7C_k^0$ for $\lambda^2 = 25$, $C_k = 0.5C_k^0$ for $\lambda^2 = 10$ and $C_k = 0.3C_k^0$ for $\lambda^2 = 5$. Figs. 6 and 7 display convergence of the volume fraction β_1 and the scaled velocities $v_k/\mathcal{V}_k$ to the incompressible limit as $\lambda \to \infty$, for $\lambda^2 = 100,\ 25,\ 10,\ 5$. Again use of a scaled velocity v_k/V_k would accelerate the convergence. We plot the curves $p_1 - p_2$ and $p_1^\infty - p_2^\infty$ for $t = 3.0$ in Fig. 8, for $\lambda^2 = 100,\ 25,\ 10,\ 5$. This figure establishes the convergence of the

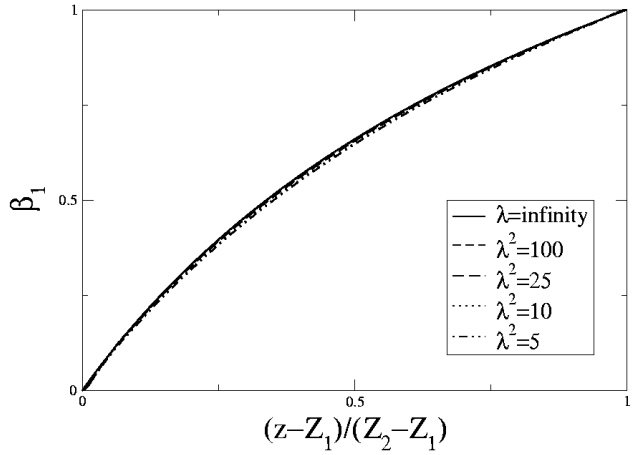

Figure 6: Convergence of the volume fraction of light fluid to the analytical incompressible solution at $t = 3.0$ as $\lambda \to \infty$.

pressure difference to the incompressible solution as $\lambda \to \infty$. Note that the $\lambda^2 = 100$ curve has crossed over the $\lambda = \infty$ curve in this limit. Due to the ill-conditioned nature of the incompressible limit when computed with a compressible code (as has been observed in some calculations not reported here), we do not believe the $\lambda^2 = 100$ calculation in Fig. 4 has sufficient accuracy to attach significance to this cross over. As shown in Fig. 4, the pressure difference is sensitive to the growth rates of compressible mixing zone, while Figs. 2 and 3 show that the volume fraction, velocities and mean pressure are insensitive. In particular, the pressure difference at the spike edge, even after scaling by $(Z_2 - Z_1)$, depends on the bubble and spike growth rates.

4.2.2 Convergence under Mesh Refinement

We conduct the simulations for $\lambda^2 = 100$ with grid sizes of 100, 200, 500 and 1000. The physical parameters are the same as those described in §4.1. We set $C_k = C_k^0$.

At time $t = 2$ the mixing zone comprises 1/4 of the computational domain, so that the coarsest $\Delta x = 1/50$ mesh, for example, has 25 cells within the mixing zone. Fig. 9 shows the convergence of the pressure difference

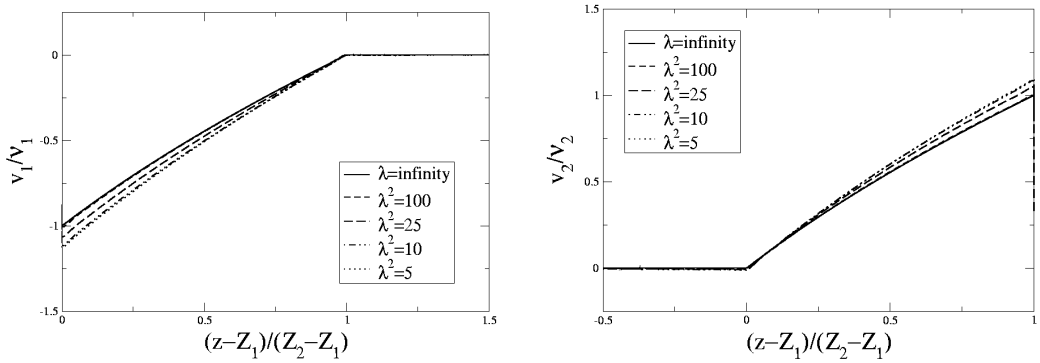

Figure 7: Convergence of the scaled velocities to the analytical incompressible solution as $\lambda \to \infty$. Here $t = 3.0$. Left: light (upper) fluid, Right: heavy (lower) fluid.

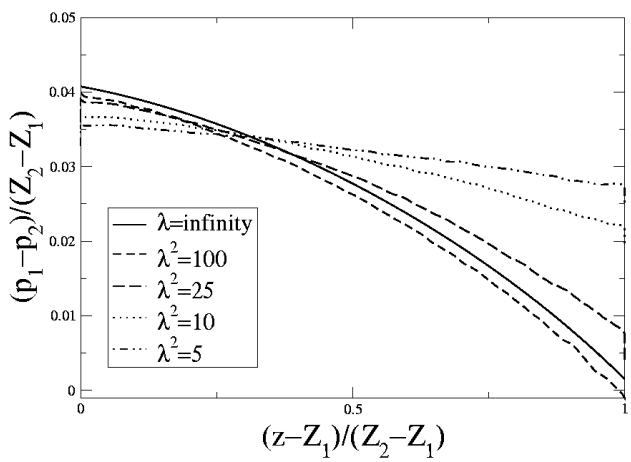

Figure 8: Convergence of the pressure difference within the mixing zone to the analytical incompressible solution as $\lambda \to \infty$. Here $t = 3.0$.

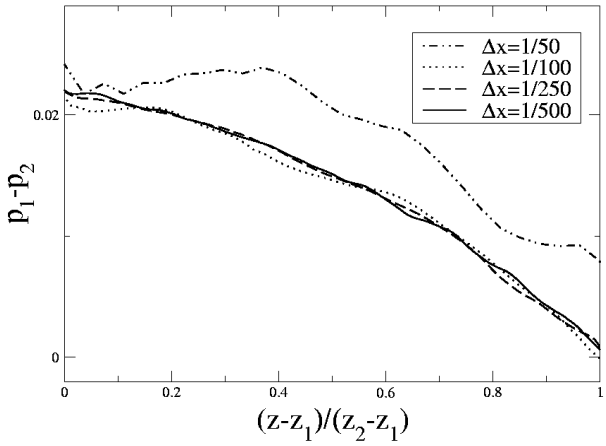

Figure 9: The convergence of the pressure difference within the mixing zone under mesh refinement. Here $\lambda^2 = 100$ and $t = 2.0$.

within the mixing zone under mesh refinement. The convergence of two fluid velocities under mesh refinement is demonstrated in Fig. 10. Since the plots of volume fraction and density are almost indistinguishable for different grid sizes, we omit them here. For the coarsest grid level shown here, the number of grid cells within the mixing zone increases from 8 to 25 over the coarse of the simulation. Note that the volume fraction, velocities and mean pressure converge much more rapidly than does the pressure difference.

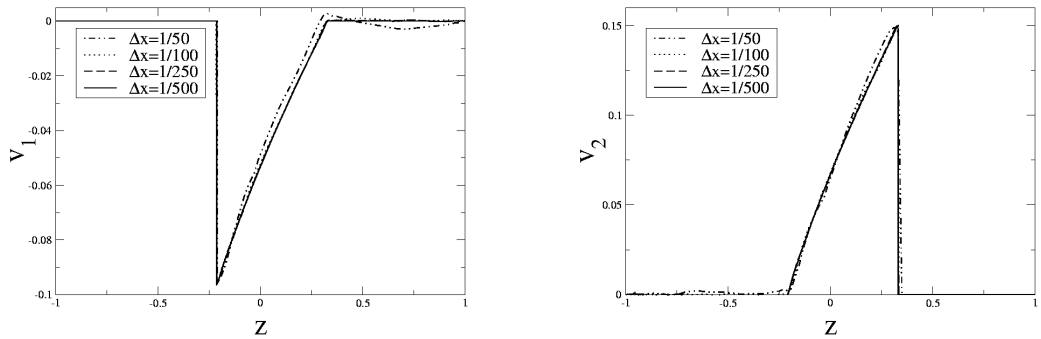

Figure 10: The convergence of the fluid velocities under mesh refinement. Here $\lambda^2 = 100$ and $t = 2.0$. Left frame: light (upper) fluid. Right frame: heavy (lower) fluid.

5 Conclusion

We have presented a numerical algorithm for the solution of the chunk mix multiphase flow equations (1) coupled to a phenomenological law (8) for the motion of the edges of the mixing layer. This algorithm extends the front tracking algorithm and deals with issues unique to the front tracking model for this multiphase model. A new analytic solution for the incompressible pressures has been described, thereby completing previous analytic solutions. The numerical algorithm has been validated by comparison to the analytic incompressible limit and by convergence under mesh refinement. The sensitive dependence of the pressure difference on the compressible drag coefficients C_k and thus on the edge motions or the mixing coefficients $\alpha_k = \alpha_k(C_k)$ has been explained in terms of the relation of the exact momentum equation evaluated at the mixing zone edge to the phenomenological buoyancy drag equation. We demonstrate insensitivity of the rest of the solution to these quantities.

Appendix A The Bubble Growth Rate α_1

Mixing rates for acceleration driven flows have been characterized by experiments, theories and simulation studies. Read and Youngs [39, 43] have published the result that the bubble acceleration rate α_1 is almost a constant, with $\alpha_1 \approx 0.063 - 0.077$ in 3-D experiments. The experiments have been repeated by various authors and similar values of α_1 have been obtained; we mention the experiments of Dimonte and Schneider [13, 15, 16] giving $\alpha_1 = 0.05 \pm 0.01$. The theoretically determined mixing rates [8, 4, 38] are obtained from a bubble merger model. They are in agreement with experiment. Three-dimensional simulations [5, 19] of the Rayleigh-Taylor instability, carried to later time, give a growth rate $\alpha_1 \approx 0.07 - 0.08$. Only the untracked (TVD) simulations [19] are in significant disagreement; careful analysis points to numerical diffusion at the contact as the cause of this discrepancy [19]. See Table 1.

Merger Models	Cheng et al. [8, 4]	$\alpha_1 \approx 0.05 - 0.06$
	Oron et al. [38]	$\alpha_1 \approx 0.05$
Experiment	Read/Youngs [39, 43]	$\alpha_1 \approx 0.063 - 0.077$
	Dimonte/Schneider [13, 15, 16]	$\alpha_1 = 0.05 \pm 0.01$
Simulation	Cheng et. al/George et al. [5, 19]	$\alpha_1 \approx 0.07 - 0.08$ (tracked) $\alpha_1 \approx 0.035$ (untracked)
	Youngs [45]	$\alpha_1 \approx 0.04 - 0.05$
	Youngs [46]	$\alpha_1 \approx 0.03$

Table 1: Values of α_1 determined from theory, experiment and simulation.

References

[1] U. Alon, J. Hecht, D. Mukamel, and D. Shvarts. Scale invariant mixing rates of hydrodynamically unstable interfaces. *Phys. Rev. Lett.*, 72:2867–2870, 1994.

[2] J. Bell, P. Colella, and J. Trangenstein. Higher order Godunov methods for general systems of hyperbolic conservation laws. *J. Comp. Phys.*, 82:362–397, 1989.

[3] Y. Chen, J. Glimm, D. Saltz, D. H. Sharp, and Q. Zhang. A two-phase flow formulation for the Rayleigh-Taylor mixing zone and its renormalization group solution. In R. Young, J. Glimm, and B. Boston, editors, *Proceedings of the Fifth International Workshop on Compressible Turbulent Mixing*. World Scientific, Singapore, 1996. ISBN 981-02-2910-0.

[4] B. Cheng, J. Glimm, H. Jin, and D. H. Sharp. Theoretical methods for the determination of mix. *Laser and Particle Beams*, 2003. submitted; Stony Brook preprint SUNYSB-AMS-02-08, LANL preprint LA-Ur-02-1440.

[5] B. Cheng, J. Glimm, X. L. Li, and D. H. Sharp. Subgrid models and DNS studies of fluid mixing. In E. Meshkov, Y. Yanilkin, and V. Zhmailo, editors, *Proceedings of the 7th International Conference on the Physics of Compressible Turbulent Mixing, (1999)*, pages 385–390, Sarov, Nizhny Novgorod region, Russia, 2001. RFNC-VNIIEF.

[6] B. Cheng, J. Glimm, D. Saltz, and D. H. Sharp. Boundary conditions for a two pressure two phase flow model. *Physica D*, 133:84–105, 1999.

[7] B. Cheng, J. Glimm, and D. H. Sharp. Density dependence of Rayleigh-Taylor and Richtmyer-Meshkov mixing fronts. *Phys. Lett. A*, 268:366–374, 2000.

[8] B. Cheng, J. Glimm, and D. H. Sharp. A 3-D RNG bubble merger model for Rayleigh-Taylor mixing. *Chaos*, 12:267–274, 2002.

[9] B. Cheng, J. Glimm, and D. H. Sharp. Multi-temperature multiphase flow model. *ZAMP*, 53:2i1–238, 2002.

[10] I-L. Chern, J. Glimm, O. McBryan, B. Plohr, and S. Yaniv. Front tracking for gas dynamics. *J. Comp. Phys.*, 62:83–110, 1986.

[11] P. Colella. A direct Eulerian MUSCL scheme for gas dynamics. *SIAM Journal on Computing*, 6(1):104–117, 1985.

[12] M. G. Crandall and A. Majda. The method of fractional steps for conservation laws. *Math. Comp.*, 34:285–314, 1980.

[13] G. Dimonte. Nonlinear evolution of the Rayleigh-Taylor and Richtmyer-Meshkov instabilities. *Phys. Plasmas*, 6(5):2009–2015, 1999.

[14] G. Dimonte. Spanwise homogeneous buoyancy-drag model for Rayleigh-Taylor mixing and experimental evaluation. *Phys. Plasmas*, 7(6):2255–2269, 2000.

[15] G. Dimonte and M. Schneider. Turbulent Rayleigh-Taylor instability experiments with variable acceleration. *Phys. Rev. E*, 54:3740–3743, 1996.

[16] G. Dimonte and M. Schneider. Density ratio dependence of Rayleigh-Taylor mixing for sustained and impulsive acceleration histories. *Phys. Fluids*, 12:304–321, 2000.

[17] D. A. Drew. Mathematical modeling of two-phase flow. *Ann. Rev. Fluid Mech.*, 15:261–291, 1983.

[18] D. Ebin. The motion of slightly compressible fluids viewed as a motion with strong constraining force. *Annals of Math*, 105(1):141–200, 1977.

[19] E. George, J. Glimm, X. L. Li, A. Marchese, and Z. L. Xu. A comparison of experimental, theoretical, and numerical simulation Rayleigh-Taylor mixing rates. *Proc. National Academy of Sci.*, 99:2587–2592, 2002.

[20] J. Glimm, J. W. Grove, X. L. Li, W. Oh, and D. H. Sharp. A critical analysis of Rayleigh-Taylor growth rates. *J. Comp. Phys.*, 169:652–677, 2001.

[21] J. Glimm, J. W. Grove, X.-L. Li, K.-M. Shyue, Q. Zhang, and Y. Zeng. Three dimensional front tracking. *SIAM J. Sci. Comp.*, 19:703–727, 1998.

[22] J. Glimm, J. W. Grove, X.-L. Li, and D. C. Tan. Robust computational algorithms for dynamic interface tracking in three dimensions. *SIAM J. Sci. Comp.*, 21:2240–2256, 2000.

[23] J. Glimm, J. W. Grove, X.-L. Li, and N. Zhao. Simple front tracking. In G.-Q. Chen and E. DiBebedetto, editors, *Contemporary Mathematics*, volume 238, pages 133–149. Amer. Math. Soc., Providence, RI, 1999.

[24] J. Glimm and H. Jin. An asymptotic analysis of two-phase fluid mixing. *Bol. Soc. Bras. Mat.*, 32:213–236, 2001.

[25] J. Glimm, D. Marchesin, and O. McBryan. Subgrid resolution of fluid discontinuities II. *J. Comp. Phys.*, 37:336–354, 1980.

[26] J. Glimm, D. Saltz, and D. H. Sharp. A general closure relation for incompressible mixing layers induced by interface instabilites. In G. Jourdan and L. Houas, editors, *Proceedings of the Sixth International Workshop on the Physics of Compressible Turbulent Mixing*, pages 179–184. Imprimerie Caractère, Marseille, France, 1997.

[27] J. Glimm, D. Saltz, and D. H. Sharp. Statistical evolution of chaotic fluid mixing. *Phys. Rev. Lett.*, 80(4):712–715, 1998.

[28] J. Glimm, D. Saltz, and D. H. Sharp. Two-pressure two-phase flow. In G.-Q. Chen, Y. Li, and X. Zhu, editors, *Nonlinear Partial Differential Equations*. World Scientific, Singapore, 1998.

[29] J. Glimm, D. Saltz, and D. H. Sharp. Two-phase modeling of a fluid mixing layer. *J. Fluid Mech.*, 378:119–143, 1999.

[30] J. W. Grove. The interaction of shock waves with fluid interfaces. *Adv. Appl. Math.*, 10:201–227, 1989.

[31] J. C. V. Hansom, P. A. Rosen, T. J. Goldack, P. Fieldhouse K. Oades, N. Cowperthwaite, D. L. Youngs, N. Mawhinney, and A. J. Baxter. Radiation driven planar foil instability and mix experiments at the AWE HELEN laser. *Laser and Particle Beams*, 8:51–71, 1990.

[32] D. Hoff. The zero-mach limit of compressible flows. *Commun. Math. Phys.*, 192:543–554, 1998.

[33] H. Jin. *The Incompressible Limit of Compressible Multiphase Flow Equations*. PhD thesis, SUNY at Stony Brook, 2001.

[34] S. Klainerman and A. Majda. Singular limits of quasilinear hyperbolic systems with large parameters and the incompressible limit of compressible fluids. *Comm. Pure Appl. Math.*, 34:481–524, 1981.

[35] S. Klainerman and A. Majda. Compresible and incompressible fluids. *Comm. Pure Appl. Math.*, 35:629–651, 1982.

[36] L. Landau and E. Lifshitz. *Fluid Mechanics*. Addison Wesley, Reading, MA, 1959.

[37] P. Lax and B. Wendroff. Systems of conservation laws. *Comm. Pure Appl. Math.*, 13:217, 1960.

[38] D. Oron, L. Arazi, Kartoon D, A. Rikanati, U. Alon, and D. Shvarts. Dimensionality dependence of the Rayleigh-Taylor and Richtmyer-Meshkov instability late-time scaling laws. *Phys. of Plasmas*, 8:2883–2889, 2001.

[39] K. I. Read. Experimental investigation of turbulent mixing by Rayleigh-Taylor instability. *Physica D*, 12:45–58, 1984.

[40] R. Richtmyer and K. Morton. *Difference Methods for Initial Value Problems.* Interscience, New York, second edition, 1967.

[41] S. L. Soo. *Particulates and Continuum: Multiphase Fluid Dynamics.* Hemisphere, New York, 1989.

[42] G. Strang. Accurate partial difference methods II: nonlinear problems. *Numer. Math.*, 6:37, 1964.

[43] D. L. Youngs. Numerical simulation of turbulent mixing by Rayleigh-Taylor instability. *Physica D*, 12:32–44, 1984.

[44] D. L. Youngs. Modeling turbulent mixing by Rayleigh-Taylor instability. *Physica D*, 37:270–287, 1989.

[45] D. L. Youngs. Three-dimensional numerical simulation of turbulent mixing by Rayleigh-Taylor instability. *Phys. Fluids A*, 3:1312–1319, 1991.

[46] D. L. Youngs. Private communication. 1999.